

Article

# Study of Metal–Semiconductor–Metal $\text{CH}_3\text{NH}_3\text{PbBr}_3$ Perovskite Photodetectors Prepared by Inverse Temperature Crystallization Method

Lung-Chien Chen <sup>1,\*</sup>, Kuan-Lin Lee <sup>1</sup>, Kun-Yi Lee <sup>2</sup>, Yi-Wen Huang <sup>1</sup> and Ray-Ming Lin <sup>3,\*</sup><sup>1</sup> Department of Electro-optical Engineering, National Taipei University of Technology, 1, 3 Sec., Chung-Hsiao E. Rd., Taipei 10608, Taiwan; zwl44@yahoo.com.tw (K.-L.L.); wendy930906@gmail.com (Y.-W.H.)<sup>2</sup> Department of Electrical Engineering, China University of Science and Technology, Taipei 11581, Taiwan; kelvin119@gmail.com<sup>3</sup> Department of Electronics, Chang Gung University, Wen-Hwa 1st Road, Kwei-Shan, Tao-Yuan 33302, Taiwan\* Correspondence: ocean@ntut.edu.tw (L.-C.C.); rmlin@mail.cgu.edu.tw (R.-M.L.);  
Tel.: +886-2-27712171 (ext. 4634) (L.-C.C.)

Received: 11 December 2019; Accepted: 3 January 2020; Published: 5 January 2020



**Abstract:** Numerous studies have addressed the use of perovskite materials for fabricating a wide range of optoelectronic devices. This study employs the deposition of an electron transport layer of  $\text{C}_{60}$  and an Ag electrode on  $\text{CH}_3\text{NH}_3\text{PbBr}_3$  perovskite crystals to complete a photodetector structure, which exhibits a metal–semiconductor–metal (MSM) type structure. First,  $\text{CH}_3\text{NH}_3\text{PbBr}_3$  perovskite crystals were grown by inverse temperature crystallization (ITC) in a pre-heated circulator oven. This oven was able to supply uniform heat for facilitating the growth of high-quality and large-area crystals. Second, the different growth temperatures for  $\text{CH}_3\text{NH}_3\text{PbBr}_3$  perovskite crystals were investigated. The electrical, optical, and morphological characteristics of the perovskite crystals were analyzed by X-ray diffraction (XRD), scanning electron microscopy (SEM), ultraviolet-visible spectroscopy, and photoluminescence (PL). Finally, the  $\text{CH}_3\text{NH}_3\text{PbBr}_3$  perovskite crystals were observed to form a contact with the Ag/ $\text{C}_{60}$  as the photodetector, which revealed a responsivity of 24.5 A/W.

**Keywords:**  $\text{CH}_3\text{NH}_3\text{PbBr}_3$  perovskite crystals; inverse temperature crystallization; large-area crystals; MSM photodetectors

## 1. Introduction

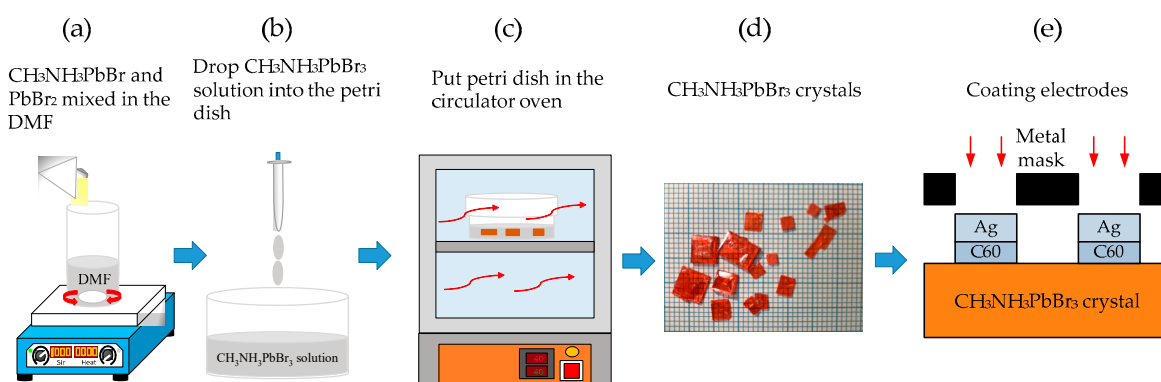
Perovskite is a material that comprises an ABX<sub>3</sub> structure. In this molecular formula, A, B, and X represent an alkali metal ion or a methylamine radical ( $\text{CH}_3\text{NH}_3$ ), a metal cation ( $\text{Pb}_2$ ,  $\text{Sn}_2$ ), and a halogen cation (Cl-, Br-, I-), respectively. Compared with organic semiconductor materials, perovskite materials based on organic metal halides exhibit unique optical and electrical properties. It is well-established that the exciton binding energy of perovskite materials is extremely small; therefore, the majority of the excitons, which are generated after being excited by light, can be separated to form free electrons and holes at room temperature. Further, the carrier current possesses a fast diffusion speed and a long diffusion distance. The diffusion lengths of electrons and holes vary with the crystal structure. Compared with MAPbI<sub>3</sub>, MAPbBr<sub>3</sub> has a shorter lattice constant, higher cohesion energy, lower phase transition temperature, and superior anisotropy [1]. The energy gap is approximately 2.2 eV, and the emission wavelength is green [2]. It has a significantly high optical gain and can be used as a gain dielectric layer in laser [3]. Perovskite materials have been successfully developed in light-emitting diodes [4–7] and solar cells [8–12]. Perovskite materials can be utilized for a wide range of applications in the field of optoelectronics. Thus far, various types of light sensors have been studied

and consequently applied; these include various photodetectors and Schottky barrier diodes [13–25]. Metal–semiconductor–metal (MSM) structured light sensors or photodetectors have the advantages of a straightforward manufacturing process, high sensitivity, and high response speed as compared with sensors possessing other structures.

Therefore, this study employs  $\text{CH}_3\text{NH}_3\text{PbBr}_3$  perovskite crystals prepared by inverse temperature crystallization method. Conventional crystallization methods, such as the typical cooling or antisolvent vapor-assisted crystallization techniques, are time-consuming and have a long process period. In contrast, the inverse temperature crystallization (ITC) is a fast solution-based crystal growth method, and the optical, electrical, and crystal properties were comparable to the results of them [26–28].  $\text{C}_{60}/\text{Ag}$  electrodes were formed to produce a MSM structure for its required research path. The optoelectronic properties of the MSM-type  $\text{CH}_3\text{NH}_3\text{PbBr}_3$  perovskite photodetectors were then examined.

## 2. Materials and Methods

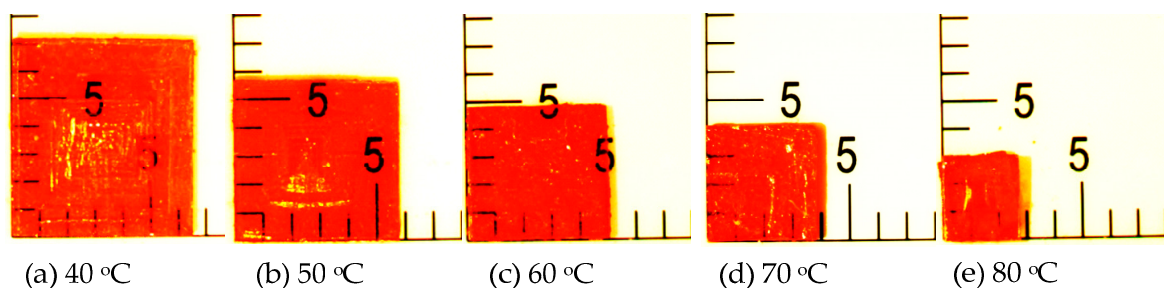
First of all, the  $\text{CH}_3\text{NH}_3\text{PbBr}_3$  perovskite precursor solution was prepared with the incorporation of 0.0367 g  $\text{PbBr}_2$  (99.998%), 0.0112 g  $\text{CH}_3\text{NH}_3\text{Br}_2$  (MAB, 99.9%), and 1 mL of dimethylformamide (DMF, 98%) solvent. Subsequently, the precursor solution was stirred until it turned clear. The Petri dishes were sonicated with acetone, alcohol, and isopropyl alcohol for 10 min. The precursor solution was then poured into the Petri dish and placed in the hot circulator oven at different temperatures, namely: 40 °C, 50 °C, 60 °C, 70 °C, and 80 °C.  $\text{CH}_3\text{NH}_3\text{PbBr}_3$  crystals were found to grow at a slow rate and gradually became larger during the crystal growth. Finally, the electron transport layer of 20 nm-thick  $\text{C}_{60}$  and the 100 nm-thick Ag electrodes were deposited on  $\text{CH}_3\text{NH}_3\text{PbBr}_3$  crystals via thermal evaporation and metal mask to complete the MSM structures with an interdigital finger electrode. Figure 1 presents the schematic diagram of the MSM photodetector process procedure.



**Figure 1.** Schematic diagram of experimental procedure in this research.

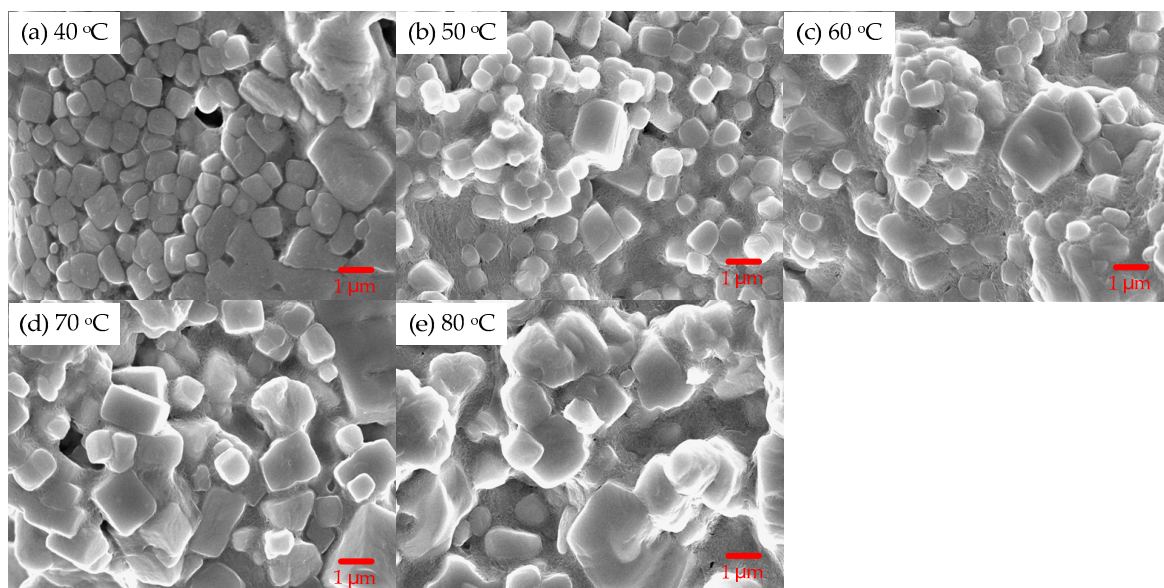
## 3. Results and Discussion

In this study, the  $\text{CH}_3\text{NH}_3\text{PbBr}_3$  precursor solution was grown in an oven until the solution completely evaporated. As shown in Figure 2, the  $\text{CH}_3\text{NH}_3\text{PbBr}_3$  crystal size was the largest under the growth temperature at 40 °C ( $45.5 \text{ mm}^2$ ). However, the  $\text{MAPbBr}_3$  crystal area gradually decreased with an increase in the growth temperature. The  $\text{CH}_3\text{NH}_3\text{PbBr}_3$  crystal area was the smallest under the growth temperature at 80 °C ( $9 \text{ mm}^2$ ). Therefore, it can be observed that the growth temperature is inversely proportional to the crystal size. A high temperature makes the solution evaporate and decrease, such that it is difficult to grow a large-sized crystal.



**Figure 2.** Pictures of  $\text{MAPbBr}_3$  crystals prepared at various temperature. The unit of scale is 1 mm.

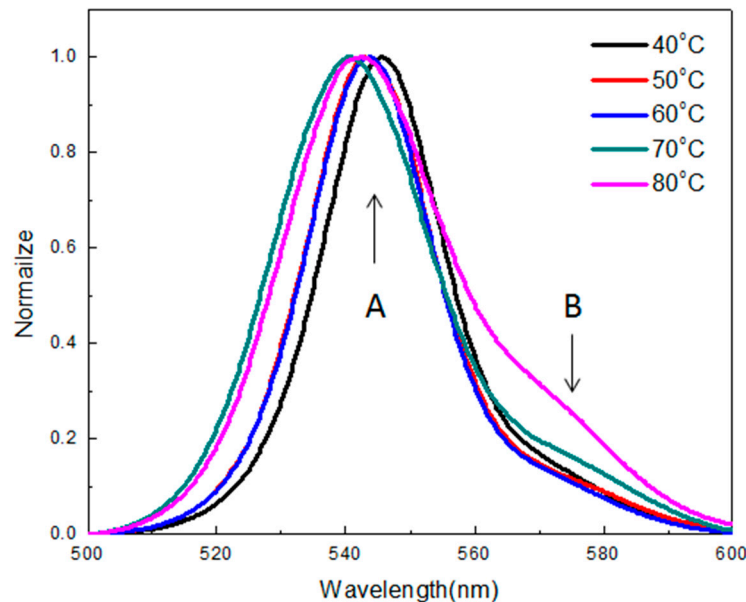
Figure 3 shows the scanning electron microscopy (SEM) images of the  $\text{MAPbBr}_3$  crystals at 40 °C, 50 °C, 60 °C, 70 °C, and 80 °C, respectively.



**Figure 3.** Scanning electron microscopy (SEM) images of the  $\text{MAPbBr}_3$  crystals growth temperature at (a) 40 °C, (b) 50 °C, (c) 60 °C, (d) 70 °C, and (e) 80 °C.

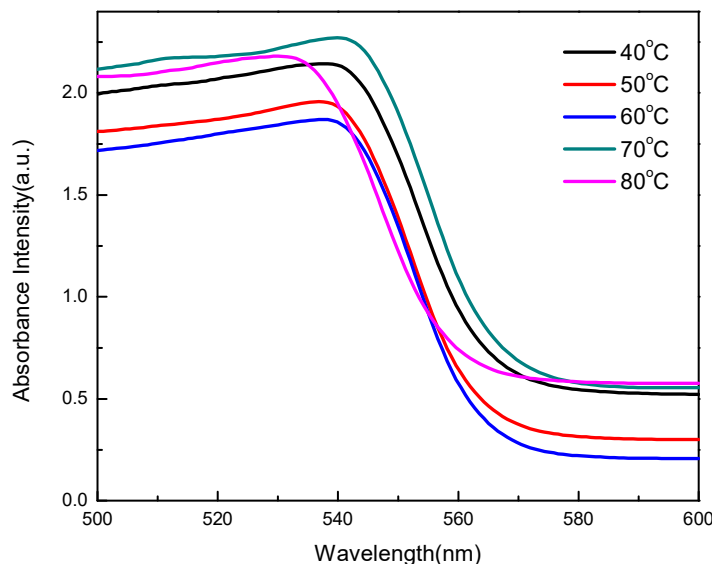
The  $\text{MAPbBr}_3$  crystal was composed of several crystal grains. The crystal obtained at 40 and 80 °C comprised many smaller and larger grains, respectively. Further, it was found that the crystal grains constituting the  $\text{MAPbBr}_3$  crystals became larger with an increase in the growth temperature.

As shown in Figure 4, the photoluminescence (PL) emission peaks of  $\text{MAPbBr}_3$  crystals were located at 545.6 nm, 543 nm, 543.6 nm, 540.6 nm, and 542.4 nm at temperatures of 40 °C, 50 °C, 60 °C, 70 °C, and 80 °C, respectively. It was observed that the peaks were in close proximity between 540 nm and 546 nm. The PL emission peak exhibited a blue shift with an increase in the growth temperature. The blue shift may be attributed to the difference in laser fluence and measurement system, as well as the atmosphere environment for characterization. [29–31]. The dominant PL peak (peak A) with the highest energy is located at ~545 nm (2.275 eV, close to band gap) with a full width at half maximum (FWHM) of ~30 nm. It is corresponding to the band-to-band transition. The lower energy peak (peak B) at ~560 nm, which had a broad bandwidth of 30 nm, was attributed to the emission of band-to-trap state (Br vacancies on the crystal surface) [32–34].



**Figure 4.** Photoluminescence (PL) spectra of the  $\text{MAPbBr}_3$  crystals prepared at various temperatures.

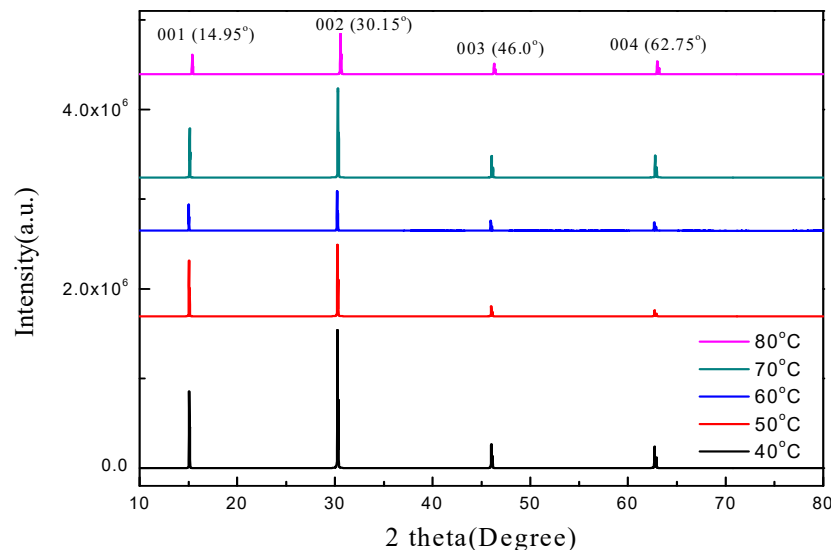
As shown in Figure 5, the edges of absorption spectra of the  $\text{MAPbBr}_3$  crystals were located at 537.58 nm, 536.83 nm, 537.58 nm, 539.85 nm, and 536.03 nm at temperatures of 40 °C, 50 °C, 60 °C, 70 °C, and 80 °C, respectively. It can be observed that the edges of absorption spectra are extremely close to one another, and that the peaks are located between 530 nm and 540 nm, corresponding to the band gap of 2.275 eV of  $\text{MAPbBr}_3$  single crystals [35].



**Figure 5.** Absorption spectra of the  $\text{MAPbBr}_3$  crystals prepared at various temperatures.

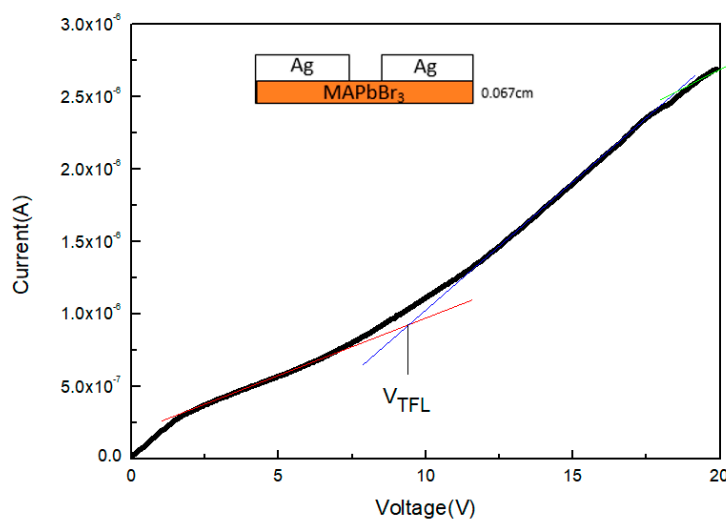
Figure 6 shows the X-ray diffraction (XRD) patterns of the  $\text{MAPbBr}_3$  crystal at 40 °C, 50 °C, 60 °C, 70 °C, and 80 °C. All growth temperatures displayed significant peaks at  $14.95^\circ$ ,  $30.15^\circ$ ,  $46.0^\circ$ , and  $62.75^\circ$ . The crystal plane directions corresponding to the cubic crystal structure were (001), (002), (003), and (004), which, in turn, correspond to high-quality  $\text{MAPbBr}_3$  crystals. When the temperature was 40 °C, the peak intensity was observed to be higher. Conversely, at 80 °C, the peak intensities were significantly lower. It can be seen from the SEM images in Figure 2 that the crystallinity and density of the sample prepared at 40 °C is the best. The peak intensity is greater than that of the samples

prepared at the temperatures of 50 to 80 °C, which is due to the lower density even though the particles are larger.



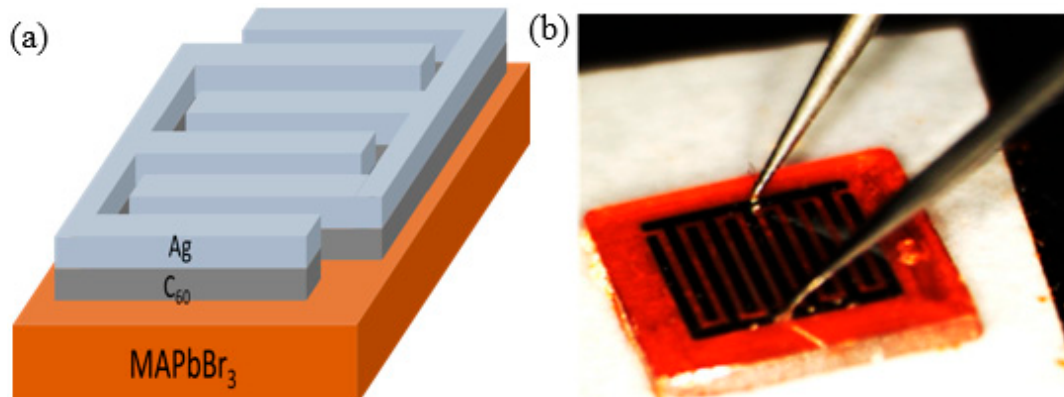
**Figure 6.** X-ray diffraction (XRD) patterns of the  $\text{MAPbBr}_3$  crystals prepared at various temperatures.

Figure 7 shows the current–voltage curve of the  $\text{MAPbBr}_3$  crystal; the red, blue, and green lines depict the Ohmic region ( $n = 1$ ), trap-filled region ( $n > 3$ ), and Child’s region ( $n = 2$ ), respectively. According to Mott-Gurney’s law:  $\mu = 8J_DL^3/9\epsilon\epsilon_0V^2$  [26,36]. Consequently, the carrier mobility of the  $\text{MAPbBr}_3$  crystal was calculated to be  $14.4 \text{ cm}^2\text{V}^{-1}\text{s}^{-1}$ . The trap density is calculated using the following equation:  $n_t = 2V_{TFL}\epsilon\epsilon_0/eL^2$ ; the trap density of  $\text{MAPbBr}_3$  crystals was  $4.7 \times 10^{10} \text{ cm}^{-3}$ .



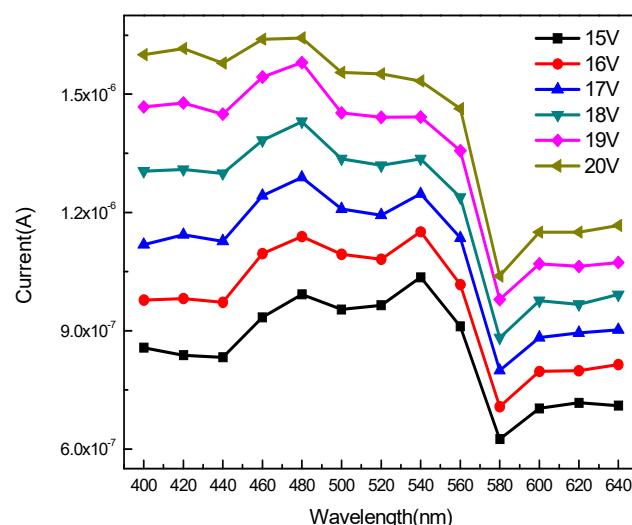
**Figure 7.** Current–voltage curve of the  $\text{MAPbBr}_3$  crystal.

The MSM structure of the  $\text{MAPbBr}_3$  crystal photodetector is shown in Figure 8a. A medium layer  $\text{C}_{60}$  was inserted between the silver (Ag) electrodes and the  $\text{MAPbBr}_3$  crystal in order to prevent from a compound of both. Figure 8b shows a photograph of the  $\text{MAPbBr}_3$  crystal with the MSM structure.



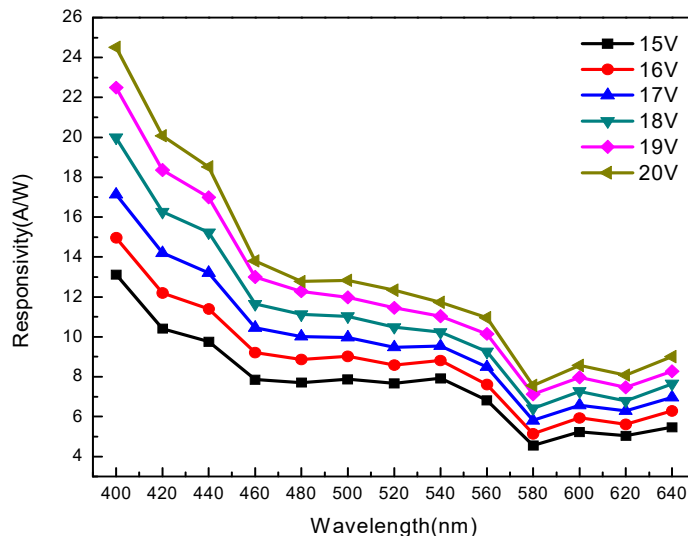
**Figure 8.** (a) Metal–semiconductor–metal (MSM) structure of the  $\text{MAPbBr}_3$  crystal photodetector. (b) Photograph of a  $\text{MAPbBr}_3$  crystal photodetector.

Figure 9 shows the current vs. wavelength graph of the photodetector under each bias. The devices exhibit high current values in the wavelength range of 400 nm to 560 nm for each bias. However, the current decreased significantly in the range of 570 nm to 580 nm. The absorption edge located at around 580 nm is corresponding to the trap level transition. The current was observed to rise slightly between 600 nm and 640 nm owing to the carrier relations from the trap in the band structure.



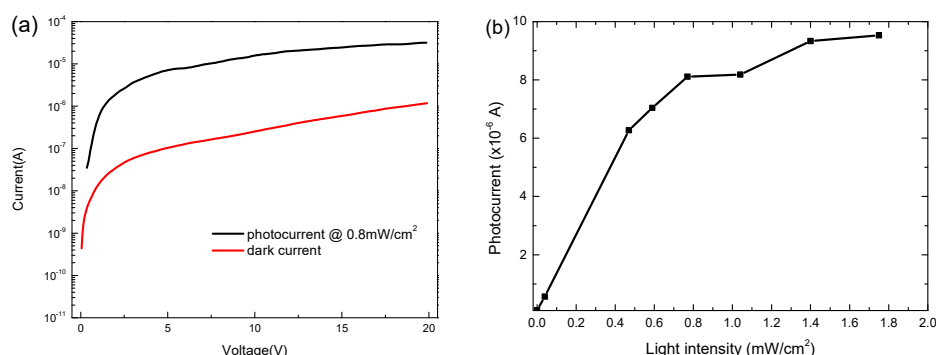
**Figure 9.** Current and wavelength curve MSM- $\text{MAPbBr}_3$  crystal photodetectors.

Figure 10 shows the wavelength and responsivity at different bias voltages. At a wavelength of 400 nm, the responsivity of the component is 13.13 A/W, 14.97 A/W, 17.13 A/W, 19.98 A/W, 22.48 A/W, and 24.50 A/W at different bias voltages of 15 V, 16 V, 17 V, 18 V, 19 V, and 20 V, respectively. From 400 nm to 460 nm, the responsivity gradually decreases and becomes stable in the range of 460 nm to 560 nm. The responsivity attained its lowest value at 580 nm, and increases slightly in the range of 600 nm to 640 nm.



**Figure 10.** Responsivity and wavelength curve of MSM-MAPbBr<sub>3</sub> crystal photodetectors.

Figure 11a plots typical dark and illuminated (under 0.8 mW/cm<sup>2</sup>) I-V characteristics of MSM-MAPbBr<sub>3</sub> crystal photodetectors at a bias ranging from 0 to 20 V. The photocurrent was approximately  $7.04 \times 10^{-6}$  A, and the dark current was approximately  $1.04 \times 10^{-7}$  A at a bias of 5 V. In this research, a relatively high dark current is a result of leakage current from the boundary in the crystal. However, a large photocurrent-to-dark-current contrast ratio is observed—at almost two orders of magnitude. The orders of magnitude of the photocurrent-to-dark-current contrast ratio were similar to other structures in other studies [37–39]. As shown in Figure 11b, the photocurrent density at −5 V was measured under different illumination intensities of a 200 W Xe lamp as the light source in order to study the dependence of the photocurrent on the incident light intensity. A linear relationship was observed when the intensity of incident light power was lower than 0.8 mW/cm<sup>2</sup>. However, when the light intensity was higher than 0.8 mW/cm<sup>2</sup>, the photocurrent was saturated owing to the balance between generation and recombination of electron–hole pairs.



**Figure 11.** (a) Current–Voltage (I–V) characteristics and (b) dynamic range of the MSM-MAPbBr<sub>3</sub> crystal photodetector under illumination of 0.8 mW/cm<sup>2</sup> and measured at 5 V.

#### 4. Conclusions

In this study, MAPbBr<sub>3</sub> crystals were grown at low temperatures using an improved inverse temperature crystallization method. It was observed that the small single crystals obtained at different growth temperatures became larger as the temperature increased; however, the crystal size was found to decrease as the temperature increased. In all single crystals, the sample prepared at temperature 80 °C showed the smallest size; the single crystal prepared at 40 °C was observed to have the largest size. The XRD pattern revealed four significantly high peaks, which were associated with high-quality MAPbBr<sub>3</sub> crystals. The PL emission peak was obtained between 536 nm to 538 nm. The absorption

edge was located at 580 nm and corresponded to the trap-level transition. The photocurrent increased slightly from 600 to 640 nm, which had been caused by the carrier relations from the trap level.

**Author Contributions:** L.-C.C. wrote the paper and designed the experiments. L.-C.C., K.-Y.L., and R.-M.L. analyzed the data. K.-L.L. and Y.-W.H. prepared the samples and performed all measurements. All authors have read and agreed to the published version of the manuscript.

**Funding:** This research was funded by the Ministry of Science and Technology of the Republic of China, grant number MOST 108-2211-E-027-093.

**Conflicts of Interest:** The authors declare no conflict of interest.

## References

1. Hata, T.; Giorgi, G.; Yamashita, K.; Caddeo, C.; Mattoni, A. Development of a Classical Interatomic Potential for MAPbBr<sub>3</sub>. *J. Phys. Chem. C* **2017**, *121*, 3724–3733. [[CrossRef](#)]
2. Chen, H.; Zheng, X.; Li, Q.; Yang, Y.; Xiao, S.; Hu, C.; Bai, Y.; Zhang, T.; Wong, K.S.; Yang, S. An amorphous precursor route to the conformable oriented crystallization of CH<sub>3</sub>NH<sub>3</sub>PbBr<sub>3</sub> in mesoporous scaffolds: Toward efficient and thermally stable carbon-based perovskite solar cells. *J. Mater. Chem. A* **2016**, *4*, 12897–12912. [[CrossRef](#)]
3. Deschler, F.; Price, M.; Pathak, S.; Klintberg, L.E.; Jarausch, D.D.; Higler, R.; Hüttner, S.; Leijtens, T.; Stranks, S.D.; Snaith, H.J.; et al. High Photoluminescence Efficiency and Optically Pumped Lasing in Solution-Processed Mixed Halide Perovskite Semiconductors. *J. Phys. Chem. Lett.* **2014**, *5*, 1421–1426. [[CrossRef](#)] [[PubMed](#)]
4. Wang, H.C.; Wang, W.; Tang, A.C.; Tsai, H.Y.; Bao, Z.; Ihara, T.; Yarita, N.; Tahara, H.; Kanemitsu, Y.; Chen, S.; et al. High-Performance CsPb<sub>1-x</sub>Sn<sub>x</sub>Br<sub>3</sub> Perovskite Quantum Dots for Light-Emitting Diodes. *Angew. Chem. Int. Ed. Engl.* **2017**, *56*, 13650–13654. [[CrossRef](#)] [[PubMed](#)]
5. Cho, H.; Kim, J.S.; Yun, H.J.; Bae, J.S.; Heo, J.; Ahn, S.; Lee, T.; Wolf, C. High-Efficiency Solution-Processed Inorganic Metal Halide Perovskite Light-Emitting Diodes. *Adv. Mater.* **2017**, *29*, 1700579. [[CrossRef](#)]
6. Li, J.; Xu, L.; Wang, T.; Song, J.; Chen, J.; Xue, J.; Dong, Y.; Cai, B.; Shan, Q.; Han, B.; et al. 50-Fold EQE Improvement up to 6.27% of Solution-Processed All-Inorganic Perovskite CsPbBr<sub>3</sub> QLEDs via Surface Ligand Density Control. *Adv. Mater.* **2017**, *29*, 1603885. [[CrossRef](#)]
7. Zhu, Z.; Zhao, D.; Chueh, C.C.; Shi, X.; Li, Z.; Jen, A.K.Y. Highly Efficient and Stable Perovskite Solar Cells Enabled by All-Crosslinked Charge-Transporting Layers. *Joule* **2018**, *2*, 168–183. [[CrossRef](#)]
8. Yang, W.S.; Park, B.W.; Jung, E.H.; Jeon, N.J.; Kim, Y.C.; Lee, D.U.; Shin, S.S.; Seo, J.; Kim, E.K.; Noh, J.H.; et al. Iodide management in formamidinium-lead-halide-based perovskite layers for efficient solar cells. *Science* **2017**, *356*, 1376–1379. [[CrossRef](#)]
9. Cai, M.; Ishida, N.; Li, X.; Yang, X.; Noda, T.; Wu, Y.; Xie, F.; Naito, H.; Fujita, D.; Han, L. Control of Electrical Potential Distribution for High-Performance Perovskite Solar Cells. *Joule* **2018**, *2*, 296–306. [[CrossRef](#)]
10. McMeekin, D.P.; Sadoughi, G.; Rehman, W.; Eperon, G.E.; Saliba, M.; Hörantner, M.T.; Haghighirad, A.; Sakai, N.; Korte, L.; Rech, B.; et al. A mixed-cation lead mixed-halide perovskite absorber for tandem solar cells. *Science* **2016**, *351*, 151–155. [[CrossRef](#)]
11. Chen, Z.; Dong, Q.; Liu, Y.; Bao, C.; Fang, Y.; Lin, Y.; Tang, S.; Wang, Q.; Xiao, X.; Bai, Y.; et al. Thin single crystal perovskite solar cells to harvest below-bandgap light absorption. *Nat. Commun.* **2017**, *8*, 1890. [[CrossRef](#)] [[PubMed](#)]
12. Bao, C.; Chen, Z.; Fang, Y.; Wei, H.; Deng, Y.; Xiao, X.; Li, L.; Huang, J. Low-Noise and Large-Linear-Dynamic-Range Photodetectors Based on Hybrid-Perovskite Thin-Single-Crystals. *Adv. Mater.* **2017**, *29*, 1703209. [[CrossRef](#)] [[PubMed](#)]
13. Wei, H.; Fang, Y.; Mulligan, P.; Chuirazzi, W.; Fang, H.H.; Wang, C.; Ecker, B.R.; Gao, Y.; Loi, M.A.; Cao, L.; et al. Sensitive X-ray detectors made of methylammonium lead tribromide perovskite single crystals. *Nat. Photonics* **2016**, *10*, 333–339. [[CrossRef](#)]
14. Saidaminov, M.I.; Adinolfi, V.; Comin, R.; Abdelhady, A.L.; Peng, W.; Dursun, I.; Yuan, M.; Hoogland, S.; Sargent, E.H.; Bakr, O.M. Planar-integrated single-crystalline perovskite photodetectors. *Nat. Commun.* **2015**, *6*, 8724. [[CrossRef](#)] [[PubMed](#)]

15. Liu, Y.; Zhang, Y.; Yang, Z.; Yang, N.; Ren, X.; Pang, L.; Liu, S.F. Thinness- and Shape-Controlled Growth for Ultrathin Single-Crystalline Perovskite Wafers for Mass Production of Superior Photoelectronic Devices. *Adv. Mater.* **2016**, *28*, 9204–9209. [[CrossRef](#)]
16. Gao, L.; Zeng, K.; Guo, J.; Ge, C.; Du, J.; Zhao, Y.; Chen, C.; Deng, H.; He, Y.; Song, H.; et al. Passivated Single-Crystalline  $\text{CH}_3\text{NH}_3\text{PbI}_3$  Nanowire Photodetector with High Detectivity and Polarization Sensitivity. *Nano Lett.* **2016**, *16*, 7446–7454. [[CrossRef](#)]
17. Chandrasekar, P.V.; Yang, S.; Hu, J.; Sulaman, M.; Shi, Y.; Saleem, M.I.; Tang, Y.; Jiang, Y.; Zou, B.; Muhammad, I.S. Solution-phase, template-free synthesis of  $\text{PbI}_2$  and  $\text{MAPbI}_3$  nano/microtubes for high-sensitivity photodetectors. *Nanoscale* **2019**, *11*, 5188–5196. [[CrossRef](#)]
18. Chen, L.C.; Weng, C.Y. Optoelectronic Properties of  $\text{MAPbI}_3$  Perovskite/Titanium Dioxide Heterostructures on Porous Silicon Substrates for Cyan Sensor Applications. *Nanoscale Res. Lett.* **2015**, *10*, 404. [[CrossRef](#)]
19. Yalcin, M.; Ozmen, D.; Yakuphanoglu, F. Perovskite cobaltates/p-silicon heterojunction photodiodes. *J. Alloys Compd.* **2019**, *796*, 243–254. [[CrossRef](#)]
20. Tian, C.; Wang, F.; Wang, Y.; Yang, Z.; Chen, X.; Mei, J.; Liu, H.; Zhao, D. Chemical Vapor Deposition Method Grown All-Inorganic Perovskite Microcrystals for Self-Powered Photodetectors. *ACS Appl. Mater. Interfaces* **2019**, *11*, 15804–15812. [[CrossRef](#)]
21. Cifci, O.S.; Koçyiğit, A.; Sun, P. Perovskite/p-Si photodiode with ultra-thin metal cathode. *Superlattices Microstruct.* **2018**, *120*, 492–500. [[CrossRef](#)]
22. Luo, W.; Yan, L.; Liu, R.; Zou, T.; Zhang, S.; Liu, C.; Dai, Q.; Chen, J.; Zhou, H. High detectivity ITO/organolead halide perovskite Schottky photodiodes. *Semicond. Sci. Technol.* **2019**, *34*, 074004. [[CrossRef](#)]
23. Pandey, K.; Chauhan, M.; Bhatt, V.; Tripathi, B.; Yadav, P.; Kumar, M. High-performance self-powered perovskite photodetector with a rapid photoconductive response. *RSC Adv.* **2016**, *6*, 105076–105080. [[CrossRef](#)]
24. Lee, W.; Lee, J.; Yun, H.; Kim, J.; Park, J.; Choi, C.; Kim, D.C.; Seo, H.; Lee, H.; Yu, J.W.; et al. High-Resolution Spin-on-Patterning of Perovskite Thin Films for a Multiplexed Image Sensor Array. *Adv. Mater.* **2017**, *29*, 1702902. [[CrossRef](#)] [[PubMed](#)]
25. Liu, Z.; Li, H.; Qin, C.; Zhang, T.; Gu, Y.; Chen, H.; Zheng, H.; Li, S. Solution-Processed Inorganic Perovskite Flexible Photodetectors with High Performance. *Nanoscale Res. Lett.* **2019**, *14*, 284. [[CrossRef](#)] [[PubMed](#)]
26. Maculan, G.; Sheikh, A.D.; Abdelhady, A.L.; Saidaminov, M.I.; Haque, A.; Murali, B.; Alarousu, E.; Mohammed, O.F.; Wu, T.; Bakr, O.M.  $\text{CH}_3\text{NH}_3\text{PbCl}_3$  Single Crystals: Inverse Temperature Crystallization and Visible-Blind UV-Photodetector. *J. Phys. Chem. Lett.* **2015**, *6*, 3781–3786. [[CrossRef](#)]
27. Dang, Y.; Liu, Y.; Sun, Y.; Yuan, D.; Liu, X.; Lu, W.; Liu, G.; Xia, H.; Tao, X. Bulk crystal growth of hybrid perovskite material  $\text{CH}_3\text{NH}_3\text{PbI}_3$ . *CrystEngComm* **2015**, *17*, 665–670. [[CrossRef](#)]
28. Shi, D.; Adinolfi, V.; Comin, R.; Yuan, M.; Alarousu, E.; Buin, A.; Chen, Y.; Hoogland, S.; Rothenberger, A.; Katsiev, K.; et al. Low trap-state density and long carrier diffusion in organolead trihalide perovskite single crystals. *Science* **2015**, *347*, 519–522. [[CrossRef](#)]
29. Fang, H.H.; Adjokatse, S.; Wei, H.; Yang, J.; Blake, G.R.; Huang, J.; Even, J.; Loi, M.A. Ultrahigh sensitivity of methylammonium lead tribromide perovskite single crystals to environmental gases. *Sci. Adv.* **2016**, *2*, e1600534. [[CrossRef](#)]
30. Qiu, Y.H.; Nan, F.; Wang, Q.; Liu, X.D.; Ding, S.J.; Hao, Z.H.; Zhou, L.; Wang, Q.Q. Tuning the Competitive Recombination of Free Carriers and Bound Excitons in Perovskite  $\text{CH}_3\text{NH}_3\text{PbBr}_3$  Single Crystal. *J. Phys. Chem. C* **2017**, *121*, 6916. [[CrossRef](#)]
31. Murali, B.; Dey, S.; Abdelhady, A.L.; Peng, W.; Alarousu, E.; Kirmani, A.R.; Cho, N.; Sarmah, S.P.; Parida, M.R.; Saidaminov, M.I.; et al. Surface restructuring of hybrid perovskite crystals. *ACS Energy Lett.* **2016**, *1*, 1119. [[CrossRef](#)]
32. Wu, X.; Trinh, M.T.; Niesner, D.; Zhu, H.; Norman, Z.; Owen, J.S.; Yaffe, O.; Kudisch, B.J.; Zhu, X.Y. Trap States in Lead Iodide Perovskites. *J. Am. Chem. Soc.* **2015**, *137*, 2089–2096. [[CrossRef](#)] [[PubMed](#)]
33. Mante, P.A.; Stoumpos, C.C.; Kanatzidis, M.G.; Yartsev, A. Electron-acoustic phonon coupling in single crystal  $\text{CH}_3\text{NH}_3\text{PbI}_3$  perovskites revealed by coherent acoustic phonons. *Nat. Commun.* **2017**, *8*, 14398. [[CrossRef](#)] [[PubMed](#)]
34. Wu, K.; Bera, A.; Ma, C.; Du, Y.; Yang, Y.; Li, L.; Wu, T. Temperature-dependent excitonic photoluminescence of hybrid organometal halide perovskite films. *Phys. Chem. Chem. Phys.* **2014**, *16*, 22476–22481. [[CrossRef](#)] [[PubMed](#)]

35. Han, L.; Liu, C.; Wu, L.; Zhang, J. Observation of the growth of MAPbBr<sub>3</sub> single-crystalline thin film based on space-limited method. *J. Cryst. Growth* **2018**, *501*, 27–33. [[CrossRef](#)]
36. Chen, L.C.; Lee, K.L.; Lin, S.E. Observation of Hybrid MAPbBr<sub>3</sub> Perovskite Bulk Crystals Grown by Repeated Crystallizations. *Crystals* **2018**, *8*, 260. [[CrossRef](#)]
37. Liu, C.; Wang, K.; Yi, C.; Shi, X.; Du, P.; Smith, A.W.; Karim, A.; Gong, X. Ultrasensitive solution-processed perovskite hybrid photodetectors. *J. Mater. Chem. C* **2015**, *3*, 6600–6606. [[CrossRef](#)]
38. Lee, S.W.; Choi, K.J.; Kang, B.H.; Lee, J.S.; Kim, S.W.; Kwon, J.B.; Gopalan, S.A.; Bae, J.H.; Kim, E.S.; Kwon, D.H.; et al. Low dark current and improved detectivity of hybrid ultraviolet photodetector based on carbon-quantum-dots/zinc-oxide-nanorod composites. *Org. Electron.* **2016**, *39*, 250–257. [[CrossRef](#)]
39. Lee, S.W.; Cha, S.H.; Choi, K.J.; Kang, B.H.; Lee, J.S.; Kim, S.W.; Kim, J.S.; Jeong, H.M.; Gopalan, S.A.; Kwon, D.H.; et al. Low Dark-Current, High Current-Gain of PVK/ZnO Nanoparticles Composite-Based UV Photodetector by PN-Heterojunction Control. *Sensors* **2016**, *16*, 74. [[CrossRef](#)]



© 2020 by the authors. Licensee MDPI, Basel, Switzerland. This article is an open access article distributed under the terms and conditions of the Creative Commons Attribution (CC BY) license (<http://creativecommons.org/licenses/by/4.0/>).